



Counting Carbon: Quantifying Biomass in the McMurdo Dry Valleys through Orbital & Field Observations

Mark R. Salvatore pa, John E. Barrett pb, Schuyler R. Borges pa, Sarah N. Power pb, Lee F. Stanish pc, Eric R. Sokol pcd and Michael N. Gooseff pce

^aDepartment of Astronomy and Planetary Science, Northern Arizona University, Flagstaff, AZ, USA; ^bDepartment of Biological Sciences, Virginia Polytechnic Institute and State University, Blacksburg, VA, USA; ^cInstitute of Arctic and Alpine Research (INSTAAR), University of Colorado Boulder, CO, USA; ^dBattelle, National Ecological Observatory Network (NEON), Boulder, CO, USA; ^eDepartment of Civil, Environmental and Architectural Engineering, University of Colorado Boulder, USA

ABSTRACT

We use correlative field studies and high-resolution multispectral remote sensing data from the WorldView-2 instrument to estimate the abundance of photosynthetically active biomass (photoautotrophs consisting primarily of microbial mats and mosses) in Canada Stream in Taylor Valley, McMurdo Dry Valleys (MDV), Antarctica. In situ field investigations were performed to (1) acquire ground validation targets for atmospherically correcting satellite imagery, (2) derive spectra of "pure" geologic and biological endmembers, (3) estimate photoautotroph cover from remote sensing data, and (4) convert these coverage estimates to biomass using data collected in the field. Our results suggest that, on the morning of 12 December 2018, the Canada Stream system contained more than 3,800 kg of photosynthetically active carbon. Extrapolating our unmixing results to the entirety of the Fryxell basin of Taylor Valley, Antarctica, we model the presence of more than 750,000 kg of photosynthetically active carbon across the landscape and carbon fixation rates roughly equivalent to five hectares of tropical rainforest. The ability to spatially and temporally quantify the amount of photosynthetically active biomass using remote sensing data in the MDV of Antarctica is a revolutionary development that will help elucidate the ecological drivers and environmental responses in this cold desert landscape.

1.0 Introduction

Ice-free regions of Antarctica are among the most extreme terrestrial environments on Earth, with the McMurdo Dry Valleys (MDV) representing some of the best studied examples of these landscapes. Persistent cold temperatures and hyper-arid conditions exemplify this polar desert landscape: liquid water is rare, precipitation (primarily in the form of snow) rarely accumulates for more than a few hours at a time, and there is an absence of macro-scale vegetation. As a result, this seemingly barren landscape is minimally impacted by biological influences that dominate most terrestrial landscapes. In

addition, seasonal variations in environmental conditions are dramatic (Doran et al. 2002). Summer conditions are characterized by perpetual daylight, temperatures near (and periodically above) freezing, and high ultraviolet (UV) radiation fluxes resulting from the polar ozone hole. These conditions promote the melting of snow, glacial ice, and subsurface ice for ~6–10 weeks per year, charging the environment with the most limiting ecological resource in the MDV: liquid water (McKnight et al. 1999; Barrett et al., 2008; Wlostowski et al. 2016; Niederberger et al. 2019). In contrast, winter conditions are beset by perpetual darkness, temperatures near -50°C, wind speeds that can regularly reach 100 miles per hour, and the complete absence of liquid water in terrestrial environments.

Despite these extreme environmental conditions, unique biological communities composed of prokaryotes, protists, and invertebrates occupy the MDV and are welladapted to the extreme environmental seasonality (Takacs-Vesbach et al. 2010). MDV lakes, streams, and soils all host unique communities that are adapted to survive in the harsh Antarctic environment (Wynn-Williams 1996; Alger et al., 1997; McKnight et al. 1999; Fritsen et al., 2000; Barrett et al. 2006; Kohler et al. 2015; Zhang et al. 2015; Van Horn et al. 2016). While the diversity and function of these communities has been extensively investigated by the McMurdo Dry Valleys Long-Term Ecological Research (MCM LTER) Programme and other researchers, quantifying biomass and productivity throughout the region has been historically difficult. This is, in part, because of the "patchiness" of these communities throughout the landscape and their rapid response to changes in the availability of organic and inorganic materials, sunlight, and liquid water (Moorhead et al. 1999; Virginia and Wall 1999; Niederberger et al. 2019). Fountain et al. (1999) describe the MDV as an "extremely climate-sensitive environment," where small changes in environmental conditions can have large effects on ecosystem dynamics. This is highlighted by processes including cryptobiosis, where ecosystems can suspend critical biological functions when environmental conditions become unfavourable, only to recover within minutes (Vincent and Howard-Williams 1986; Hawes, Howard-Williams, and Vincent 1992; McKnight et al. 2007; Kohler et al. 2015). Aeolian redistribution of biological materials has also been shown to result in variations in both the abundance and composition of biotic communities throughout Taylor Valley (Nkem et al. 2006; Michaud, Šabacká, and Priscu 2012). This "patchiness" (in space, time, and composition) of ecological communities throughout the MDV makes it difficult to accurately quantify primary production and biomass in the MDV without the ability to resolve all three dimensions of ecosystem dynamics.

The eastern end of Taylor Valley of the MDV has been particularly well studied because of the diversity of soil biota and the numerous meltwater streams, which exhibit seasonal variability of environmental conditions. Specifically, the area surrounding perennially frozen Lake Fryxell (hereafter, the Fryxell basin) has been shown to host a variety of soil and stream communities that exhibit high degrees of spatial and temporal variations in water availability and soil properties (Gooseff et al. 2017). Photoautotrophic communities composed of cyanobacteria, eukaryotic microalgae, and mosses are the most conspicuous of these communities, as they form spatially coherent mats within and near ephemeral stream channels and lake margins. Each community is uniquely adapted to survive and take advantage of microenvironmental conditions that are present throughout the basin (Alger et al., 1997; Kohler et al. 2015). For example, microbial mat communities dominated by the desiccation-resistant cyanobacterial genus *Nostoc* (colloquially and broadly

referred to as "black mats") dominate the exposed subaerial margins of stream channels where they are less likely to be scoured by high stream flow (Kohler et al. 2015). Alternatively, microbial mats dominated by Oscillatoria and Phormidium genera (referred to as "orange mats") primarily occupy the higher flow thalwegs of stream channels where they are more firmly anchored to the streambed. Nostoc and Oscillatoria comprise the most areally abundant microbial mat communities found in the Fryxell basin (Alger et al., 1997), while "green mats" (dominated by the green algal genus Prasiola) and "red mats" (dominated by Oscillatoria, Phormidium, and Leptolyngbya) are generally less abundant (Alger et al., 1997). These algal mats are clearly growing during the austral summer as daily pulses of meltwater generate enough shear stress to cause sloughing and release of mat material (Cullis, Stanish, and McKnight 2014), instigating re-growth. Mosses (dominated by the genus Bryum) are also widespread throughout Taylor Valley, primarily occupying landscape positions that are intermittently wet like stream margins and soils influenced by snow packs (Schwarz, Green, and Seppelt 1992; Seppelt et al. 1992; Alger et al., 1997; McKnight and Tate 1997; Ball and Virginia 2014).

In this study, we build on previous studies (Salvatore 2015; Power et al. 2020; Salvatore et al. 2020) to develop and validate a means of quantifying the distribution and abundance of photosynthetically active terrestrial biomass throughout the Fryxell basin using high-resolution multispectral satellite data, concurrent spectral validation in the field, and spectral mixture analysis (SMA) techniques. We are able to remotely characterize these active photoautotrophic communities because of the absence of vascular plant canopies. Significant spectral differences between these communities and underlying geologic materials simplifies our remote sensing efforts relative to other more complex ecological systems. Despite this relative simplicity, the rapid changes in ecosystem processes and photoautotroph response to local environmental conditions requires coordinated spatial and spectral validation efforts. Beyond this instantaneous characterization of photoautotrophic communities throughout the Fryxell basin, our work develops a critically important "Rosetta Stone" for remotely quantifying biomass in the MDV using validated orbital data and remote sensing techniques that can be implemented when concurrent field validation is not possible.

2.0 Study Region

Taylor Valley in the MDV is an approximately WSW-ENE trending glacial valley with its mouth approximately 80 km northwest of McMurdo Station. To the west, Taylor Valley is bounded by Taylor Glacier, which originates from the East Antarctic Ice Sheet. To the east, the valley broadens towards Explorer's Cove located on the McMurdo Sound. Between Taylor Glacier and the McMurdo Sound, Taylor Valley hosts three main topographic basins that contain permanently ice-covered lakes fed by streams that drain meltwater from nearby glaciers: Lake Bonney to the west, Lake Hoare in the centre, and Lake Fryxell (Figure 1) to the east. From west to east, these basins transition from narrower with steeper walls to broader and more shallow slopes in the Fryxell basin. A result of this broadening is that meltwater streams can reach a greater width and length in the Fryxell basin than any other sub-basin in Taylor Valley, which also facilitates a greater abundance of stream-fed ecosystems.

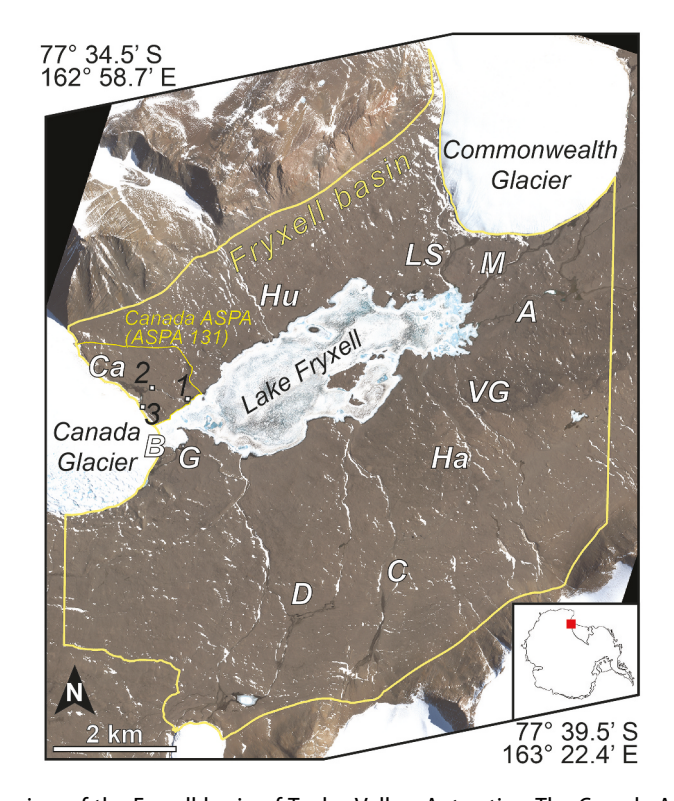


Figure 1. An overview of the Fryxell basin of Taylor Valley, Antarctica. The Canada Antarctic Specially Protected Area (ASPA) and three spectral sampling grids, indicated by black numbers, can be seen to the east of Canada Glacier. Ca = Canada Stream, Hu = Huey Creek, LS = Lost Seal Stream, M = McKnight Creek, A = Aiken Creek, VG = Von Guerard Stream, Ha = Harnish Creek, C = Crescent Stream, D = Delta Stream, G = Green Creek, and B = Bowles Creek. Data © 2018 DigitalGlobe, Inc.

Lake Fryxell is fed by eleven meltwater streams that are intermittently active for up to ~10 weeks of the year during the peak solar illumination and temperatures of the austral summer (Alger et al., 1997). The channels range in morphology from broad and braided to highly incised with steep slopes, with channel floors also ranging from sand- to cobble-dominated. Discharge from each stream channel is extremely variable and intermittent relative to temperate streams, and is dependent on several variables, most notably air temperature and solar insolation at their source (Conovitz et al. 1998; Wlostowski et al. 2016). The variability in morphology and activity of these stream systems significantly influences their resident communities, with greater biomass present in broad flat streams with cobble-dominated beds and more consistent discharge (Alger et al., 1997).

Canada Stream is located northwest of Lake Fryxell, draining the eastern margins of Canada Glacier into Lake Fryxell down a relatively steep (0.041 m m⁻¹) topographic gradient (Figure 2). The stream hosts a wide range of morphological and hydrological settings, from relatively flat and braided expanses, to large ponds, to deeply incised and narrow channels, to anastomosing channels within a deltaic formation at the terminus of the stream (McKnight and Tate 1997). This diversity, in addition to the regularity of fluvial activity of this system, fuels one of the densest

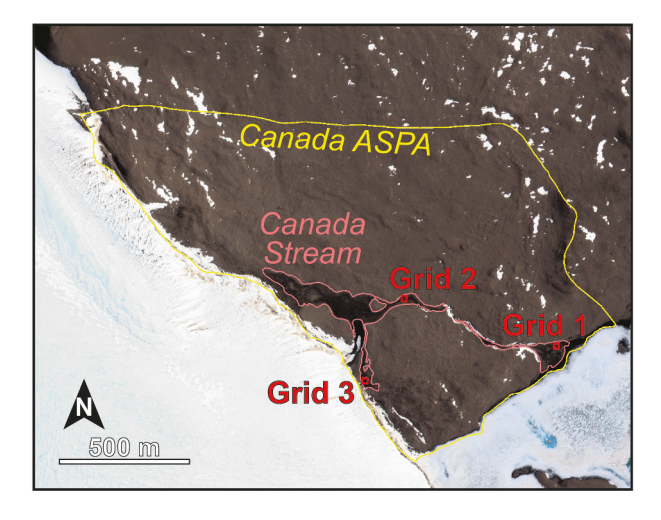


Figure 2. A closer view of the Canada ASPA, with Canada Stream and the three spectral sampling grids identified. Data © 2018 DigitalGlobe, Inc.

and most biologically diverse ecosystems in the entirety of the MDV (McKnight and Tate 1997), which led to its designation as an Antarctic Specially Protected Area (ASPA; Seppelt et al. 1992).

A WorldView-2 (WV02) image of the Fryxell basin was acquired on 12 December 2018 at 08:00:21 local time (11 December 2018 21:00:21 GMT), approximately 1 h after our team began collecting field data in the Canada ASPA. Field spectra were collected in three predetermined grids within the Canada Stream system (**Figs. 1** and **2**). Grid 1 is located in the Canada Stream delta, which is dominated by patchy distributions of primarily black and orange microbial mat communities with spatially limited exposures of green mat and moss. Grid 2 is located in the main channel of Canada Stream approximately 200 m upstream of the stream gauge maintained by the MCM LTER Programme. At the time of this study, Grid 2 was dominated by shallow flowing water (~10–30 cm depth) with a mixture of sand, cobbles, and orange microbial mats along the streambed. Grid 3 is located in the heavily vegetated region adjacent to Canada Glacier known as the "Flush," which is dominated largely by black microbial communities and mosses that occupy saturated sandy and pebbly substrates (Seppelt et al. 1992; Power et al. 2020).

3.0 Methods

3.1 Field Methods

3.1.1 Reflectance Spectroscopy

Reflectance spectra were acquired in the field for three primary applications: orbital image calibration, surface endmember characterization, and spectral comparison with orbital data over ecological regions of interest. Prior to our field campaign, grids of 20 m \times 20 m with individual points 5 m apart were established using ArcGIS and previously collected WV02 multispectral data over areas of variable biological coverage as well as invariant geologic landscapes (e.g., Figure 3). The invariant geologic surfaces were used to

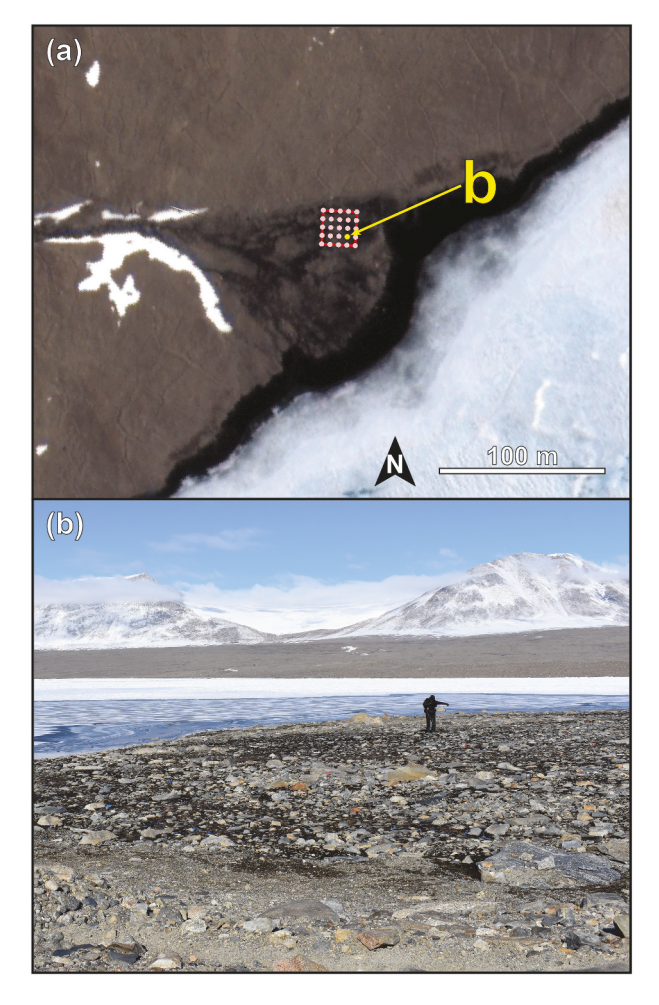


Figure 3. (a) A pan-sharpened view of Grid 1 in the delta of Canada Stream. Each individual point represents a spectral sampling location. The yellow dot indicates the location of (b), which is where the investigator is collecting data from in the photograph. Data © 2018 DigitalGlobe, Inc. Photograph courtesy of MRS.

calibrate orbital data to surface reflectance (see below), while the other grids were designed to capture the full range of spectral signatures over different types of ecosystems.

At each of the 25 individual points per grid, 150 individual spectra were acquired in three orientations relative to the direction of solar illumination. Data were collected at shoulder height above the surface and at arm's length from the collector, who only wore matte black clothing during spectral collection to minimize the risk of spurious scattering into the spectrometer (Figure 3b). Data were only collected under cloud-free conditions to minimize indirect atmospheric scattering and for the best comparison to orbital data. In addition to spectral grids, spectra of archetypal geologic materials and photoautotrophic communities were also acquired. These spectra were acquired to represent the full range of potential spectral endmembers that might be present in orbital multispectral data.

Field spectra were acquired using a portable visible/near-infrared FieldSpec4 Hi-Res field spectrometer manufactured by Analytical Spectral Devices, Inc. (now Malvern Panalytical). This hyperspectral instrument collects data between 0.35 µm and 2.50 µm over 2,151 spectral bands, with a spectral sampling of 1 nm and a resolution of 3 nm and 8 nm over the visible and near-infrared wavelength ranges, respectively. Data were calibrated to surface reflectance using a Spectralon white reference at least once every 20 min or whenever solar illumination conditions were observed to change. Spectralon contains weak absorption features at 2.14 µm and 2.43 µm (Clark et al. 1990; Zhang et al. 2014), which can be empirically removed by multiplying the resultant reflectance spectra by the measured Spectralon reference spectrum. This simple empirical correction is effective for most field applications (Zhang et al. 2014). Once acquired, spectral data were individually investigated for spectral artefacts or issues before being averaged as an entire grid. This average spectrum was then interpreted to represent the surface signature that should be observable from orbit at that specific location. Hyperspectral field data were downsampled to WV02 bandpasses using the spectral bandpass information contained in Updike and Comp (2010), making it possible to directly compare these data to those derived from the WV02 instrument.

Lastly, downsampled field spectra were linearly unmixed using a library derived from *in situ* spectra of pure geologic and biological materials, which served as spectral "end-members" in our efforts to model their abundances (Figure 4). We use a linear SMA to mathematically model the spectral contribution of individual surface components present at the subpixel level (Lawson and Hanson 1974; Adams, Smith, and Gillespie 1993; Ramsey and Christensen 1998; Salvatore et al. 2020). SMA linearly combines a library of "pure"

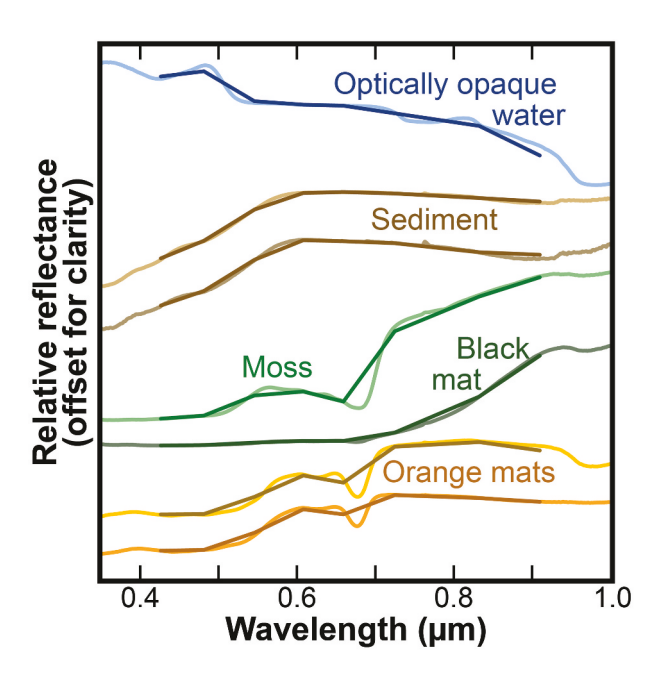


Figure 4. Spectral endmembers used in our linear unmixing models. Hyperspectral field data are shown in lighter lines, with the darker lines representing the data following downsampling to WorldView-2 resolutions. Data are offset for clarity.

spectral endmembers to match the measured spectral signature while reducing the misfit between measured and modelled spectra, recorded as the root-mean-square (RMS) error. The reflectance (R) measured for each band (R) at each pixel (R) is modelled as the sum of reflectance values for all combined endmembers (integers R) through R) in each band, weighted by their areal abundance in that pixel (R). The residual error between the measured reflectance spectrum and the model result at each wavelength (R) is also calculated, providing the ability to quantify the model's goodness of fit as its RMS error. There is also a constraint that requires all endmember fractions to sum to unity (1.0), which indicates that each pixel is made entirely of a combination of the provided endmembers:

$$R(\lambda)_{p} = \sum_{i=1}^{n} \zeta_{i} R(\lambda)_{i} + \delta(\lambda) \cdot \sum_{i=1}^{n} \zeta_{i} = 1.0$$
 (1)

Linear SMA is appropriate for this investigation because volumetric and multiple scattering is relatively small in this environment, which is dominated by optically opaque geologic and photoautotrophic endmembers (Roberts, Adams, and Smith 1993; Peddle, Hall, and LeDrew 1999; Salvatore et al. 2020). Endmember libraries for use with linear SMA can contain up to eight spectral endmembers, which is restricted based on the number of spectral bands and degrees of freedom in the data that are being unmixed (Adams, Smith, and Gillespie 1993; Ramsey and Christensen 1998). We chose to first downsample our hyperspectral data to the eight WV02 spectral bands to ensure consistency between our field and orbital observations, as one of the goals of this investigation is to determine the accuracy of remote sensing techniques for ecological observations in the MDV. Our chosen endmember library (Table 1 and Figure 4) contained seven individual endmembers that were representative of both the surrounding landscape and the photoautotrophic communities present within the Canada Stream system. Desiccated and inactive microbial mat and moss communities were not included in our endmember library, as the diagnostic spectral features found in actively photosynthesizing communities are significantly reduced in desiccated communities, becoming largely indistinguishable from local soils (Barták et al. 2016; Trnková and Barták 2017). As a result, our methods are only able to identify and quantify the abundance of active photosynthetic biomass and not the total amount of active and inactive biomass that is present. The eighth spectral endmember

Table 1. Spectral endmembers used in the linear unmixing of both field and orbital data

Endmember	Date of Collection	Location of Collection	Notes
Soil #1	12/20/2018	Crescent Stream	Dry, bright
Soil #2	12/22/2018	Bowles Creek	Damp, dark
Water (Derived)	01/16/2019	Fryxell Camp	Derived from experiment to test the effect of shallow water depths on spectral signatures
Black Mat	01/10/2019	Canada Stream	Active, saturated
Moss	01/25/2019	Bowles Creek	Active, damp
Orange Mat #1	01/15/2019	Bowles Creek	Active, saturated
Orange Mat #2	01/25/2019	Bowles Creek	Active, lighter (lightly bleached)

was an artificial linear spectrum that is designed to scale the overall brightness of the surface, accounting for properties that include variations in solar illumination, topography, and surface roughness, among other factors that influence surface albedo.

Due to spectral and radiative nonlinearities present in the visible and near-infrared (VNIR) portions of the electromagnetic spectrum, linear unmixing models are typically not used on VNIR reflectance data. Instead, complex nonlinear radiative transfer modelling is most commonly used to account for these complexities (e.g., Hapke 1993). We chose to use a linear unmixing model in this investigation for several reasons. Linear models are far less computationally taxing than nonlinear models, which allows us to use this same technique to unmix both individual field spectra in addition to the tens of millions of spectra contained within a single WV02 multispectral image in relatively short order. In addition, nonlinear behaviours are typically absent or minor among most materials being modelled, as these materials are generally opaque throughout the relatively short wavelength range covered by the WV02 sensor (Rodríguez-Caballero, Escribano, and Cantón 2014). Their opacity, therefore, ensures that the areal abundance of surface materials is generally representative of the bulk volumetric abundances as well. While some photoautotrophic communities have been found to create partially transparent films, the areal distribution of these complex relationships was observed to be the exception rather than the norm. Additionally, the unmixing model used here will still be able to positively identify both spectral contributions so long as each of the biological components is provided as a spectral endmember in our library, even if the relative abundance of these components is imprecise. For these reasons, in addition to the observed consistency between field-measured surface abundances and those modelled using field spectra and remote sensing data, the use of a linear unmixing algorithm is appropriate for this work.

Our linear unmixing efforts were validated in the field using 30 cm diameter circular plots (~707 cm²) that were demarcated and measured using our field spectrometer. The abundance of different surface materials was estimated by eye to the nearest 5% and matched to the surface abundances derived using our linear unmixing technique. We analysed 29 different combinations of photoautotrophic and non-biological surface components to calculate the error between observed and modelled endmember abundances. The results of these validation efforts are presented below.

3.1.2 Biology Coverage Estimates

Estimates of the areal abundance of biological materials within the three grids in Canada Stream were made using the National Ecological Observatory Network (NEON) Digital Hemispherical Photo (DHP) protocol, which was originally designed for skyward-facing estimates of canopy cover and revised for downward-facing estimates of ground cover. As designed for the standard DHP protocol, fisheye photos were acquired at waist height with the camera positioned horizontally towards the ground using a monopod. Images were acquired in the cardinal directions at distances of 2 m, 6 m, and 10 m from the centre of each grid within the Canada Stream system, resulting in a total of 12 images from each grid.

Following DHP data acquisition, it became apparent that the software used to automate the identification of biological materials from DHP imagery was incapable of definitively differentiating between biological and nonbiological materials in these settings. Specifically, the combination of standing water, shadow, and the similar colour of the biological communities and the adjacent non-biological materials all led to inconsistent automated results that were not reproducible. Differentiating between pure microbial communities and complex mixtures of mats and mosses was also difficult given the nature of these images. Despite being less confident in our ability to differentiate between different biological communities, our methods demonstrate consistency when estimating total biological coverage. To mitigate these aforementioned issues, we refined our methods to instead perform repeated manual and automated image classifications, the combination of which allowed us to confirm that our approach produced consistent results when estimating total coverage of biology.

In our refined approach, images were subset to the central 50% of the image, minimizing the edge effects of the fisheye lens. The spatial coverage of biological materials was then estimated using various manual and automated techniques, including supervised and unsupervised classification schemes as well as manual identification. A demonstration of this DHP image analysis process can be seen in Figure 5. Data from Grid 2 in Canada Stream were deemed unusable for estimating biological coverage due to turbidity in the water that caused significant and spatially variable sun glint (Figure 6). As a result, accurate estimates of coverage could not be quantified at this grid location, and so Grid 2 was omitted from our field validation efforts and our correlative field and orbital spectroscopic study. Results for Grid 1 and Grid 3, however, are consistent between the different counting techniques.

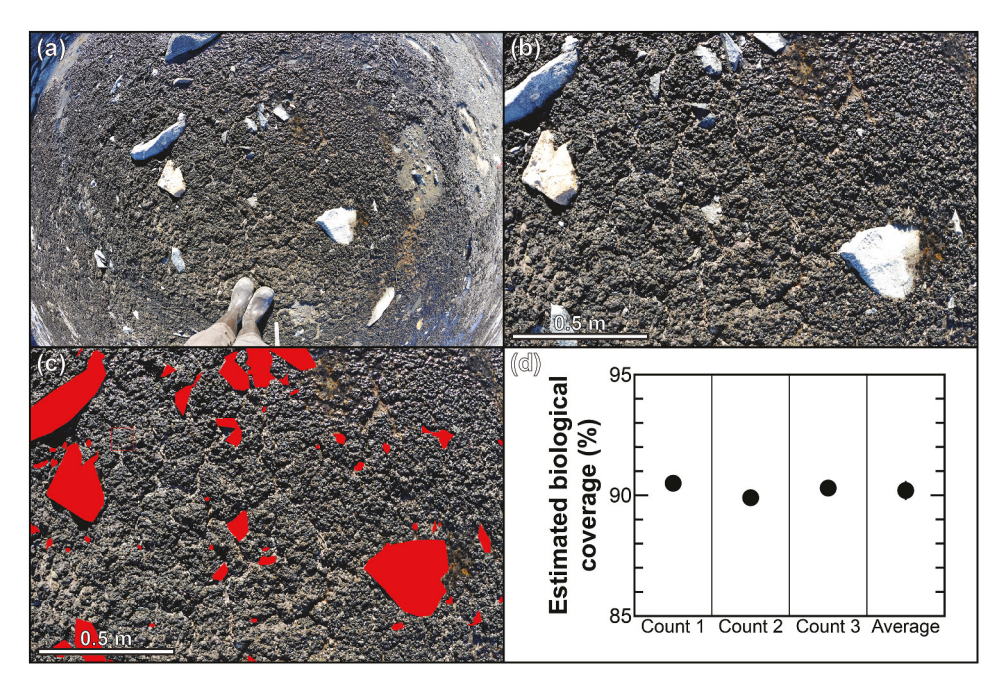


Figure 5. Illustration of the methods used to estimate surface cover of biological materials in the field. (a) Original hemispherical image. (b) Central 50% of the image. (c) Non-biological materials identified and highlighted in red, which is used to approximate the surface cover of biological materials. (d) The results from three separate estimates of biological cover for the same image, along with the average value of ~90%. Image corresponds to Photo 6910 in Grid 3 of Canada Stream. Photos courtesy of LFS.



Figure 6. An example of a digital image collected for biological cover estimates in Grid 2 of Canada Stream. The shallow flowing water creates turbidity and ripples that make it impossible to accurately estimate biological coverage. Photo courtesy of LFS.

3.1.3 Biological Sampling and Biomass Estimation

Biological samples were collected from within the Canada Stream system to derive areal estimates of biomass from different biological communities. Samples were collected from 24 locations within the three Canada Stream spectral grids: 12 black mat samples, nine orange mat samples, and three moss samples. Sampling locations were determined based on observed spatial and biological variability within the microbial mat and moss communities present in the Canada Stream system. Samples were acquired using a 13 cork borer (2.27 cm² circular plug) rinsed with deionized (DI) water. The cork borer was twisted and pressed through the entirety of the biological material until contact was made with the underlying sediments or cobbles. The biological material was then extracted using tweezers and placed in a sterile Whirl-Pak with local water from the stream (Figure 7).

Upon return to our field camp, the Whirl-Paks were emptied into filter units loaded with ashed Whatman® GF/C filters. DI water and a vacuum pump were used to facilitate the concentration of all biological material onto the filter. The filter containing the



Figure 7. A photo of an investigator sampling orange mat using a cork borer. Photo courtesy of MRS.

biological sample was then folded onto and sealed within aluminium foil, labelled, and stored in plastic petri dishes in a lab freezer at -20°C. Upon return to McMurdo Station, the filters were separated from the aluminium foil onto pre-weighed aluminium tins, dried at 100°C for 24 h, and weighed before being moved to a muffle furnace and combusted at 450°C for 5 h. Samples were reweighed to calculate ash-free dry mass (AFDM) per unit area for comparison to estimated biological surface cover from in situ and orbital measurements.

3.2 Remote Sensing

The WV02 sensor was launched by DigitalGlobe, Inc., on October 08, 2009, into a nearpolar (98.4° inclination) sun-synchronous orbit with an altitude of 770 km and an orbital period of 100.2 min (Updike and Comp 2010). The sensor consists of eight multispectral bands spanning 0.427 µm to 0.908 µm and capable of achieving a maximum spatial resolution of roughly 3.39 square meters per pixel (m²/pixel), in addition to a panchromatic band capable of achieving a maximum spatial resolution of 0.21 m²/ pixel (Updike and Comp 2010). WV02 image 1030010089D13500 was acquired from the Polar Geospatial Center (PGC) through a cooperative agreement between the National Science Foundation and the National Geospatial Intelligence Agency and was orthorectified by the PGC using their catalogue of ground control points, resulting in geographic accuracies on the order of 1-2 pixels as determined based on studies using similar techniques (Aguilar et al., 2013).

3.2.1 Image Calibration

Raw digital number (DN) data were corrected and calibrated using the ENVI image processing software and the methods described in Salvatore (2015) and Salvatore et al. (2020). Sensor- and scene-specific information required for image processing and calibration can be found in Table 2 and Table 3, respectively. DN were first converted to top-ofatmosphere spectral radiance using the following equation from Updike and Comp (2010):

$$L_{\lambda,b,p} = \frac{\left(\mathsf{K}_b \times q_{b,p}\right)}{\Delta \lambda_{b,p}} \tag{2}$$

Table 2. WorldView-2 sensor-specific information used in image calibration. From Updike and Comp (2010).

Band	Center Wavelength (μm)	Effective Bandwidth (μm)	Esun _{λ} (W m ⁻² μ m ⁻¹)
1	0.427	0.0473	1758.2229
2	0.478	0.0543	1974.2416
3	0.546	0.0630	1856.4104
4	0.608	0.0374	1738.4791
5	0.659	0.0574	1559.4555
6	0.724	0.0393	1342.0695
7	0.831	0.0989	1069.7302
8	0.908	0.0996	861.2866

Table 3. WorldView-2 scene-specific information for the data used in this study, including derived atmospheric information

			Absolute Radiometric Calibration Factor		pheric Cori Parameters	
Image	Image Properties	Band	(K _b , W m ⁻² sr ⁻¹ count ⁻¹)	Slope	Intercept	R^2
1030010089D13500	Date/Time of	1	0.01238844	0.955	-0.188	0.976
	Acquisition:	2	0.01783568	0.797	-0.122	0.999
	11 Dec. 2018	3	0.01364197	0.770	-0.056	0.995
	21:00:21 GMT	4	0.01228423	0.746	-0.021	0.991
	Earth-Sun	5	0.01851735	0.704	-0.009	0.989
	Distance:	6	0.01095514	0.648	+0.006	0.984
	0.98457 AU	7	0.02050828	0.641	+0.013	0.984
	Solar Elevation: 28.8°	8	0.01206941	0.677	+0.025	0.978

where the top-of-atmosphere spectral radiance (L_{λ}) for each band (b) at each pixel (p) is equal to the product of the absolute radiometric calibration factor for each band (K_b) and the radiometrically corrected DN in each band at each pixel $(q_{b,p})$ divided by the effective bandwidth for each band $(\Delta \lambda_{b,p})$ and applied to every pixel in the scene. These data were then converted to top-of-atmosphere reflectance using the following equation:

$$\rho_{\lambda,b,p} = \frac{L_{\lambda,b,p} \times d_{ES}^2 \times \pi}{Esun_{\lambda,b} \times \sin \theta_S}$$
(3)

where the top-of-atmosphere reflectance (ρ_{λ}) for each band (b) at each pixel (p) is equal to the product of the top-of-atmosphere spectral radiance $(L_{\lambda,b,p})$, the square of the Earth-Sun distance (d_{ES}) , and a π term that assumes a Lambertian surface, and divided by the product of the mean exoatmospheric solar irradiance calculated for each band (Esun_{λ,b}) and the sine of the solar elevation angle at the time of image acquisition (θ_S) . This calculation is again performed for each pixel in the image. Mean exoatmospheric solar irradiances were calculated using an exoatmospheric solar spectral irradiance standard (Thuillier et al., 2003).

The atmospheric contributions to this WV02 image were derived by comparing the WV02 top-of-atmosphere reflectance data to the five invariant geologic surfaces that were spectrally characterized during the 2018-2019 field campaign in Taylor Valley (Table 4). These five locations were selected based on their variable surface albedos (estimated from orbit), which provides a suitable dynamic range to determine the contributions of atmospheric scattering irrespective of surface brightness. Spectral data for each of these five grids were acquired in a manner identical to the spectral grids for biological characterization described above. Individual spectra were averaged to generate a single spectrum representative of the 20 m × 20 m surface. Data were then downsampled to WV02 resolutions and quantitatively compared with the orbital data calibrated to top-ofatmosphere reflectance. Correlations between orbitally derived top-of-atmosphere reflectance and field-derived surface reflectance were established and used to generate a suite of atmospheric corrections for the WV02 data (Table 3). WV02 data were then converted to surface reflectance by applying the band-specific correction factors to each top-ofatmosphere reflectance pixel. The accuracy of this calibration technique was confirmed using spectra of other regions within the Fryxell basin, including those containing biological and non-biological surface features. While previous studies in the Antarctic

Table 4. Locations and descriptions of the five invariant grids used for deriving atmospherically corrected surface reflectance. "B#" represents the corresponding WorldView-2 bands, where B1 denotes band 1, etc.

	Central				Field- <i>l</i>	Measure	d Refle	ctance		
Location	Coordinates	Description	B1	B2	В3	B4	B5	B6	В7	B8
Fryxell Camp	77.6048° S, 163.1295° E	Flat alluvium deposit near terminus of Huey Creek. Surface dominated by pebbles.	0.125	0.139	0.165	0.178	0.178	0.176	0.172	0.169
Green Creek	77.6237° S, 163.0587° E	Undulating surface between Green and Bowles creeks. Surface dominated by cobbles and sand.	0.113	0.128	0.154	0.169	0.171	0.170	0.165	0.161
North Fryxell	77.5959° S, 163.1559° E	Gentle slope uphill from the margin of Lake Fryxell. Surface dominated by cobbles and sand.	0.100	0.111	0.130	0.141	0.143	0.142	0.138	0.134
F6 Camp	77.6132° S, 163.2640° E	Upslope from F6 Camp. Basaltic clasts darken the surface relative to other nearby locales. Surface dominated by cobbles and sand.	0.095	0.105	0.121	0.131	0.132	0.131	0.127	0.125
Crescent Stream	77.6495° S, 163.2161° E	Flat area east of Crescent Stream. Relatively bright materials dominated by granitic and metasedimentary pebbles.	0.104	0.117	0.139	0.151	0.152	0.151	0.178	0.145

have had success using scene-derived atmospheric correction techniques for spectral comparisons and the generation of spectral parameters (Salvatore et al., 2014, Salvatore et al. 2020; Salvatore 2015; Power et al. 2020), quantitative comparisons to field-derived data necessitate validation beyond what is possible through remote scene-derived calibration efforts. However, because of numerous unique aspects of Antarctic remote sensing, including the dearth of atmospheric information, the rapidly changing weather conditions, and the extreme viewing and illumination geometries, traditional atmospheric correction techniques using radiative transfer modelling have been found to inadequately calibrate data to surface reflectance (Salvatore et al., 2014). Consequently, the use of in situ ground validation targets provides a consistent means of deriving atmospheric properties without the need to make assumptions about atmospheric conditions or to derive atmospheric spectra from scene-derived extrapolations.

3.2.2 Image Unmixing

Once calibrated to surface reflectance, each 8-band WV02 pixel was linearly unmixed using the same endmember library and methods described above for field spectra (Figure 8). The resultant dataset provides a two-dimensional view of modelled endmember abundances and RMS errors across the landscape, helping to identify whether a surface endmember was mistakenly omitted from the model. RMS errors are generally very low (typically less than 0.25%), indicating the good modelled fits between the input spectra and the modelled spectral results. Pixels where RMS errors surpassed 1% were omitted from our analyses as they indicate a lack of appropriate endmembers and typically correspond to features like snow packs or ice. Following this RMS omission,

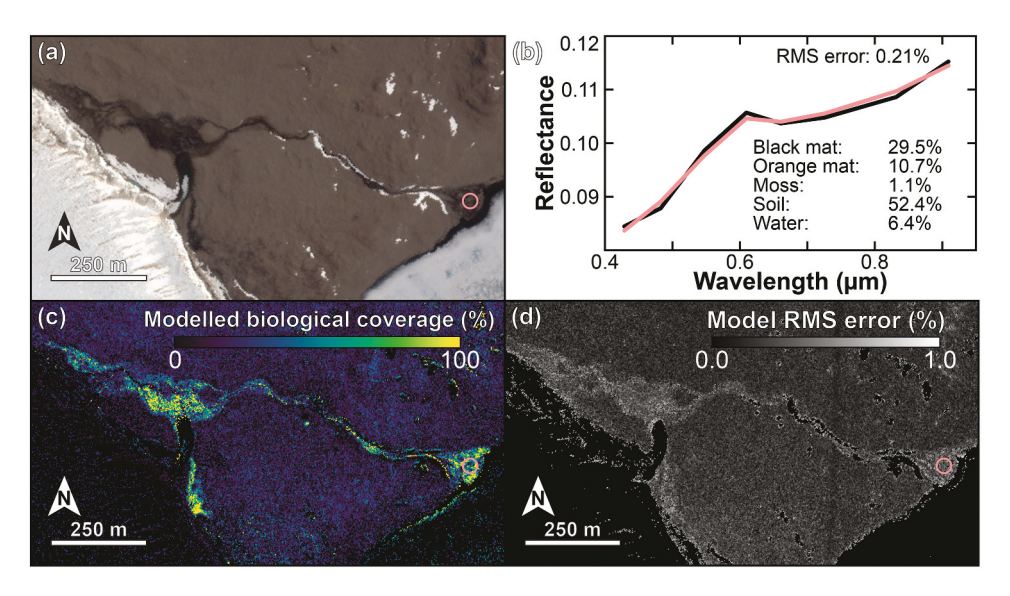


Figure 8. (a) Context image of Canada Stream. Pink circle indicates the pixels where the spectra from (b) were acquired. (b) Remotely measured (black) and spectral mixture model- (SMA-) derived modelled spectra (pink) from the delta of Canada Stream, showing a good spectral fit (RMS error of 0.21%) and reported modelled surface abundances. (c) The spatial distribution of modelled biological surface cover throughout Canada Stream. (d) The spatial distribution of model RMS errors, showing slightly higher RMS errors within Canada Stream where surface cover is more complex than the surrounding biology-poor landscape. Data © 2018 DigitalGlobe, Inc.

spatially coherent areas of higher RMS errors were still visible and were typically associated with areas of complex endmember mixtures, deeper water, snow pack or ice margins that did not meet our RMS error threshold, or other factors. However, because of the overall low RMS errors and the good fits between the input and modelled spectra, these higher RMS errors are not concerning. Our ground validation demonstrates that, despite these slightly higher RMS errors, our model results are still consistent with field observations. These results verify that our chosen endmember library was sufficiently representative of the spectral complexity observed throughout the WV02 scene.

4.0 Results

4.1 Validating Spectral Unmixing Analyses

Our linear SMA validation efforts exhibited strong correlations between the abundances of photoautotrophic materials estimated in our 30 cm-diameter circular calibration plots and model results (Figure 9), suggesting that our unmixing efforts were able to accurately quantify the abundances of different surface endmember components in both simple and complex mixtures. The coefficient of determination (R^2) value for the relationship between estimated and modelled total biomass abundances was found to be 0.97, with less than 3% disagreement between the linear relationship defined to relate the observed and modelled abundances. The average difference between the measured and modelled areal abundances of all surface biology was \pm 10.7%, which is used throughout the

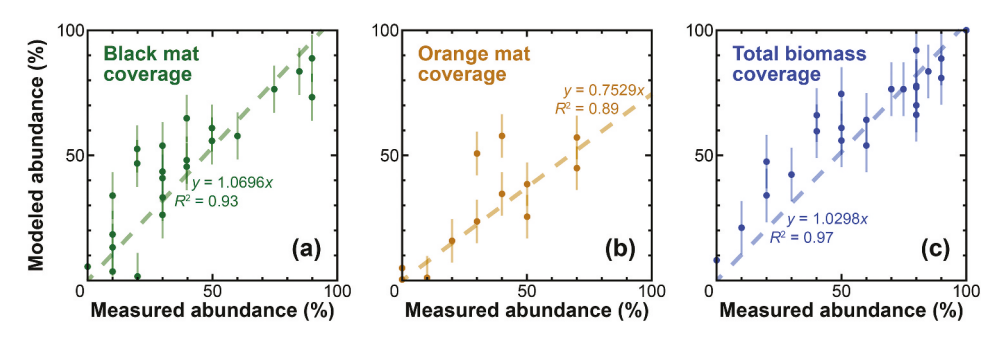


Figure 9. Comparisons between measured surface abundances of different endmembers and modelled abundances using linear unmixing. SMA models were run using the same endmember library described above. Error bars represent the average offset between measured and modelled abundances. (a) Black mat; (b) orange mat; and (c) total biomass.

remainder of this investigation as an estimate for all of our spectroscopy-based photoautotrophic community abundance estimates where scale and extent prevented direct field validation from being conducted.

4.2 Correlating Field and Remote Sensing Measurements

DHP imagery from Grid 1 and Grid 3 in the Canada Stream system were analysed to estimate total abundances (i.e., ground cover) of biological materials within these spectral grids. Photosynthetic biology was estimated to constitute $47.4 \pm 2.5\%$ and $56.9 \pm 1.8\%$ cover of Grid 1 and Grid 3, respectively (Table 5). The reported errors represent the standard deviations among the three separate abundance estimates. However, significant heterogeneity in the patchiness of biological coverage was found in each of the grids, with intra-grid variability measured at $18.1 \pm 1.7\%$ in Grid 1 and $28.3 \pm 0.4\%$ in Grid 3. These relatively high values indicate the extent of spatial variability, while the small standard deviations confirm the repeatability of our cover estimates.

Calibrated *in situ* field spectra and WV02 surface reflectance data from all three grids show remarkable spectral similarity and demonstrate the efficacy of our calibration processes (Figure 10). The ~4% higher overall reflectance observed in the orbital data relative to the field spectra may be the result of an incomplete geometric calibration when converting orbital data to surface reflectance, or potentially the result of different surface or atmospheric properties between when field validation measurements and orbital data were acquired. Regardless of this minor offset, the remarkably similar spectral shapes suggest that the spectra are accurately capturing the surface signatures as they relate to endmember abundances. Standard deviations between biological surface cover using DHP imagery, field spectra, and orbital spectra for Grid 1 and Grid 3 were calculated at 4.4% and 0.8%, respectively. Additionally, the RMS errors between measured field and orbital reflectance spectra and the derived SMA models is very low (average of 0.195%). These small errors and standard deviations all demonstrate that our linear SMA techniques and selected endmember library can accurately model the observed spectra and predict the surface abundance of biological materials (Table 6).



Table 5. Digital Hemispherical Photo- (DHP-) derived biological abundances at Grid 1 and Grid 3 within Canada Stream. Reported are both the abundances of biological materials and the techniques used to estimate their abundances for each count. Abundances could not be estimated for Grid 1 because of specular reflection and turbulence in the water. UC = Unsupervised Classification, SC = Supervised Classification, "Rocks" = quantified abundance of rocks, "Bio" = quantified abundance of mats.

		Cou	nt 1	Cour	nt 2	Coui	nt 3	Average &
Location	Photo	Biological Abundance (%)	Technique	Biological Abundance (%)	Technique	Biological Abundance (%)	Technique	Standard Deviation (SD) (%)
Grid 1	6845	73.7	UC .	73.2	Rocks	70.7	Rocks	27.5 ± 1.6
	6846	55.0	ÜC	53.8	Rocks	46.9	Bio	51.9 ± 4.4
	6847	35.9	UC	36.2	Bio	38.1	Bio	36.7 ± 1.2
	6851	71.0	Rocks	73.2	UC	63.6	Rocks	69.3 ± 5.0
	6852	76.2	Rocks	75.3	UC	67.8	Rocks	73.1 ± 4.6
	6853	62.2	Rocks	50.5	UC	50.3	Bio	54.3 ± 6.8
	6854	14.5	Bio	17.5	Bio	15.7	Bio	15.9 ± 1.5
	6855	32.8	Bio	41.7	Rocks	35.9	Bio	36.8 ± 4.5
	6856	25.1	Bio	26.6	Bio	29.3	Bio	27.0 ± 2.2
	6857	37.9	Rocks	41.3	Rocks	38.5	Bio	39.2 ± 1.8
	6858	51.5	UC	46.1	SC	37.6	Bio	45.1 ± 7.0
	6859	50.4	UC	34.5	UC	35.2	Rocks	40.0 ± 9.0
	Average	48.8		47.5		44.1		47.4 ± 2.5
	SD	19.9		18.7		16.5		18.1 ± 1.7
Grid 3	6902	17.0	UC	12.3	Bio	13.9	Bio	14.4 ± 2.4
	6903	91.8	UC	90.6	Rocks	90.4	Rocks	90.9 ± 0.7
	6904	55.8	UC	68.5	Rocks	62.8	Bio	62.4 ± 6.4
	6905	45.4	Rocks	40.6	Bio	42.6	Bio	42.8 ± 2.4
	6906	19.1	Rocks	19.2	Bio	19.3	Bio	19.2 ± 0.1
	6907	33.6	Rocks	32.2	Bio	36.0	Bio	33.9 ± 1.9
	6908	57.6	Bio	59.3	Rocks	57.0	Rocks	58.0 ± 1.2
	6909	82.8	Bio	78.2	Rocks	81.5	Rocks	80.8 ± 2.4
	6910	90.5	Bio	89.8	Rocks	90.3	Rocks	90.2 ± 0.4
	6911	76.0	Rocks	75.3	Bio	76.8	Rocks	76.1 ± 0.8
	Average SD	57.0 28.0		56.6 28.7		57.1 28.2		56.9 ± 1.8 28.3 ± 0.4

4.3 Extrapolating Beyond the Canada Stream Validation Sites

Once we have demonstrated that orbital multispectral data can be used to accurately estimate the areal coverage of actively photosynthesizing biological materials, we can expand these techniques beyond our validation sites and into the entirety of Canada Stream, the Canada ASPA, and the broader Fryxell basin (Figure 11). These broader model results are presented in Table 6. Our results suggest that, on average, the floor of Canada Stream was approximately 30% covered with actively photosynthesizing biology at the time of WV02 image acquisition. The Canada ASPA (see Figure 2) is modelled as having 12.3% cover of photosynthetic biomass, while the Fryxell basin (outlined in Figure 11 and defined as the area surrounding Lake Fryxell below 250 m elevation and bound by 162.99°E to the west and 163.36°E to the east) is modelled as having 5.7% cover by photoautotrophic communities. This basin-wide calculation contains both highly vegetated stream channels as well as relatively barren soils. Given the 53.5 km² area of the Fryxell basin (excluding Lake Fryxell itself), this equates to roughly 3.2 km² of biological surface materials, or equivalent to roughly half of the frozen extent of Lake Fryxell itself.

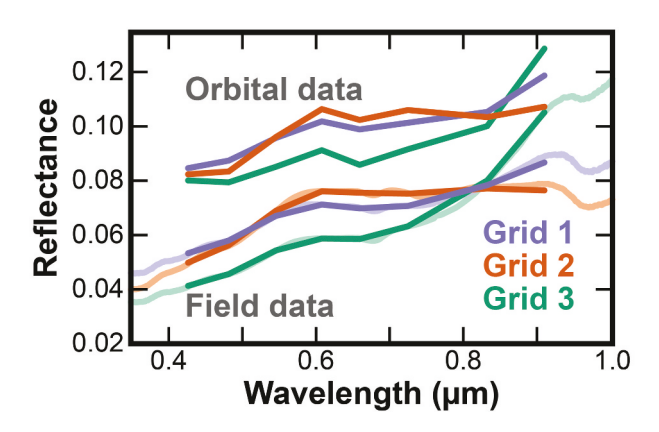


Figure 10. Field- and orbital-derived spectra from the three gridded locations in Canada Stream. Light lines represent the original hyperspectral data collected using the field spectrometer before downsampling to WorldView-2 resolutions (bold lines). Despite the ~4% offset between field and orbital data, the spectral signatures are very similar and indicate the efficacy of the WorldView-2 atmospheric correction technique.

4.4 Extrapolating Remote Sensing Data to Biomass

Our AFDM estimates are presented in Table 7 and average $0.6973 \pm 0.2740 \text{ kg m}^{-2}$ (n = 12), $0.2047 \pm 0.0548 \text{ kg m}^{-2}$ (n = 9), and $0.6627 \pm 0.2388 \text{ kg m}^{-2}$ (n = 3) for black mats, orange mats, and mosses, respectively. Because our spectral unmixing analyses report per cent abundances of each endmember, and because the size of our remote sensing pixels and field grids are known, we are able to convert these percentages to biomass using these AFDM calculations. Our calculations and error estimates suggest that the Fryxell basin contains a total photosynthetic biomass of $1.43 \times 10^6 \text{ kg } (\pm 10.7\%)$. Assuming an organic carbon content of 53% in the biological materials studied here (Wetzel, 1983; Power et al. 2020), this translates to an abundance of organic carbon of $7.57 \times 10^5 \text{ kg}$. This represents the first spatially, spectrally, and biologically validated estimate of biomass and organic carbon throughout the Fryxell basin, representing a singular snapshot in time that can be repeated using archived orbital data or data yet to be collected.

5.0 Discussion

Our spectral measurements acquired concurrently in the field and from orbit, in addition to the field sampling and surveying of photoautotrophic communities, serve as a critically valuable and complementary dataset that provides the foundation for our quantitative investigation of biomass throughout the Fryxell basin. These concurrent measurements are the only means by which it is possible to validate our remote sensing and spectral modelling efforts of these highly variable ecosystems that can respond rapidly to changing environmental conditions. Calibrating these remote sensing techniques and quantitatively demonstrating the ability to accurately model biological surface coverage and biomass allows for

Table 6. Measured and modelled photosynthetic biology coverage throughout the Fryxell basin on 12 December 2018. Reported are mean values, assumed errors based on field validation studies (Figure 9), and observed or modelled spatial variability, highlighting the heterogeneous distribution of these photosynthetic ecosystems. Values in italics and parentheses represent model RMS errors.

	Mea	sured Biol	ogical	Modelled	lelled Biological Coverage	Coverage	Modelled I	lodelled Biological Coverage	Coverage				
	ŭ	Coverage (DHP)	(JHC)	(Fj	Field Spectra)	a)	(Ort	Orbital Spectra)	ra)	Modelled Biomass (kg)	nass (kg)	Modelled Organic Carbon	c Carbon (kg)
Location	¹C (%)	^{1}C (%) ^{2}E (%) ^{3}SV (%)	3SV (%)	C (%)	E (%)	(%) AS	C (%)	E (%)	(%) AS	U	Ш	U	Ш
Grid 1	47.4	47.4 2.5 18.1	18.1	39.0%	4.2	12.1	41.0	4.4	22.4	Field: 98.5	Field: 10.5	Field: 52.2	Field: 5.6
				(0.14)			(0.24)			Satellite: 104.7	Satellite: 11.2	Satellite: 55.5	Satellite: 5.9
Grid 3	56.9	1.8	28.3	56.3	0.9	9.6	57.9	6.2	29.8	Field: 151.2	Field: 16.2	Field: 80.1	Field: 8.6
				(0.22)			(0.18)			Satellite: 142.1	Satellite: 15.2	Satellite: 75.3	Satellite: 8.1
Canada Stream							31.5	3.4	27.1	7,272.3	778.1	3,854.3	412.4
							(0.23)						
Canada ASPA							12.3	1.3	12.3	72,752.9	7,784.6	38,559.1	4,125.8
							(0.13)						
Fryxell Basin							5.7	9.0	8.0	1,428,627.2	152,863.1	757,172.4	81,017.4
							(0.12)						

C = Areal coverage. ²E = Error, estimated as 10.7% of the measured coverage based on our derived errors from field validation and spectral analyses (Figure 9). ³SV = Spatial Variability, estimated as the standard deviation of all pixels or spectral field measurements from that particular location.

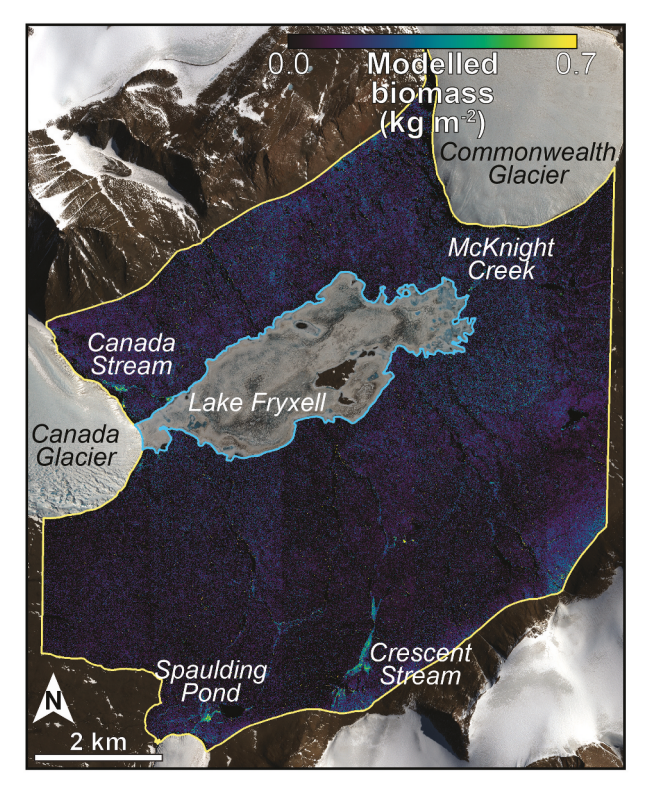


Figure 11. A map of modelled biomass across the entirety of the Fryxell basin. While individual stream channels and ponds appear to have high biomass, the vast majority of the landscape shows very low biomass abundances that, areally, are significant contributors to the overall Fryxell basin biomass. Data © 2018 DigitalGlobe, Inc.

future remote sensing investigations to do the same using our derived field validation efforts as opposed to requiring concurrent field validation. Therefore, this study validates this remote sensing technique and establishes a means of assessing the coverage of actively photosynthesizing communities and their biomass remotely over both space and time.

To determine the relative contribution of soils to the total modelled photosynthetic carbon throughout the Fryxell basin, we subset the basin into low production areas (i.e., soils) and high production areas (i.e., streams, ponds, lake margins) using a photosynthetic carbon threshold of 75 g C m⁻², which corresponds to half of the average total organic carbon abundance in Taylor Valley reported in Burkins, Virginia, and Wall (2001) (see below for a discussion corresponding to the similarities and differences between our estimates and those of previous field studies). Low production areas make up 96.25% of the basin's total surface area with an average photosynthetic carbon abundance of 18.2 \pm 19.1 g C m⁻², while high production areas make up 3.75% of the basin's total surface area with an average photosynthetic carbon abundance of 90.7 \pm 19.9 g C m⁻². Importantly, these results suggest that only 16.2% of the total modelled active photosynthetic carbon in the Fryxell basin can be found in these high production areas, while the remaining 83.8% of modelled photosynthetic carbon can be attributed to low production areas.



Table 7. Ash-free dry mass (AFDM) calculations from samples in Canada Stream. All samples were collected on 12 December 2018, the same day as the WorldView-2 and field spectral data were collected.

Location	Sample Name	Type	AFDM (g)	AFDM (kg m^{-2})
Grid 1	P01SP01	Orange Mat	0.0449	0.1978
	P01SP02	Moss	0.1178	0.5189
	P01SP03	Black Mat	0.1322	0.5824
	P01SP04	Black Mat	0.1766	0.7780
	P01SP05	Orange Mat	0.0544	0.2396
	P01SP06	Orange Mat	0.0489	0.2154
	P01SP07	Orange Mat	0.0309	0.1361
	P01SP08	Black Mat	0.1093	0.4815
	P01SP09	Orange Mat	0.0264	0.1163
	P01SP10	Black Mat	0.0789	0.3476
Grid 2	P02SP01	Black Mat	0.1921	0.8463
	P02SP02	Orange Mat	0.0674	0.2969
	P02SP03	Orange Mat	0.0482	0.2123
	P02SP04	Black Mat	0.1259	0.5546
	P02SP05	Orange Mat	0.0424	0.1868
	P02SP06	Black Mat	0.1433	0.6313
	P02SP07	Orange Mat	0.0546	0.2405
	P02SP08	Black Mat	0.0708	0.3119
Grid 3	P03SP01	Black Mat	0.1814	0.7991
	P03SP02	Moss	0.2130	0.9383
	P03SP03	Moss	0.1205	0.5308
	P03SP04	Black Mat	0.2410	1.0617
	P03SP05	Black Mat	0.1658	0.7304
	P03SP06	Black Mat	0.2821	1.2427
AVERAGES		Black Mat $(n = 12)$	0.1583 ± 0.0662	0.6973 ± 0.2740
		Orange Mat $(n = 9)$	0.0465 ± 0.0125	0.2047 ± 0.0548
		$Moss\;(n=3)$	0.1504 ± 0.0542	0.6627 ± 0.2388

On average, our estimates of total active photoautotrophic biomass and organic carbon throughout the Fryxell basin are lower than, yet comparable to, previously derived estimates using field data and broad spatial extrapolations. Our SMA results and biomass conversions estimate that the soils of Canada ASPA outside of the vegetated stream channel contains approximately 20.2 \pm 23.1 g C m⁻² in photoautotrophic biomass exposed at the surface. This is slightly lower yet congruent with the results of Barrett et al. (2006), who measured organic carbon content in Taylor Valley soils between 23 \pm 3.5 and 69 \pm 10 g C m⁻². Burkins, Virginia, and Wall (2001) derive an average Taylor Valley soil organic carbon content of ~150 g C m⁻² with a range from 37 to 260 g C m^{-2} .

Lastly, the MCM LTER Program's Soil Elevational Transect Experiment (Wall and Virginia 2005) measured organic carbon biomass in 26 soils samples from three locations in the Hoare basin and derived an average value of 11.1 \pm 2.5 μ g C g⁻¹ soil (Table 8). The WV02 image used in our study covers these sampling locations in the Hoare basin as well, and our modelled estimate over the same area was found to be $11.6 \pm 11.6 \,\mu g \, C \, g^{-1}$ soil. We derived our statistics from an average of nine pixels centred over each of the MCM LTER soil sampling locations.

All three of the above studies (Burkins, Virginia, and Wall 2001; Wall and Virginia 2005; Barrett et al. 2006) derived their soil carbon estimates using aggregated soils from the uppermost 10 cm of the surface, which integrated a much greater volume

Table 8. Comparisons between measured microbial carbon biomass at three locations in the Hoare basin of Taylor Valley by the McMurdo Dry Valleys Long-Term Ecological Research (MCM LTER) Program and that derived orbitally in this investigation. Assumes a bulk soil density of 1.85 g cm⁻³ (Burkins, Virginia, and Wall 2001) and a homogeneous abundance of organic carbon throughout the soil column. Reported orbital values are a 3×3 pixel average surrounding the central pixel as a means of estimating error.

Location	Sample Microbial Carbon Biomass ($\mu g \ C \ g^{-1}$ Soil)	Orbitally Modelled Organic Carbon ($\mu g \ C \ g^{-1}$ Soil)
77.63282° S, 162.88940° E	12.4 ± 2.2	11.5 ± 8.4
77.63553° S, 162.88931° E	9.8 ± 1.7	9.3 ± 13.4
77.63763° S, 162.88661° E	11.0 ± 2.9	13.9 ± 12.7
AVERAGE	11.1 ± 2.5	11.6 ± 11.6

of soil (and organic carbon) per square meter than our remote sensing approaches. Reflectance spectroscopy is only sensitive to the uppermost optical surface (typically less than 1 mm), which is the likely reason for the discrepancy between our estimates and previously derived estimates. Our large model error is likely the result of both spatial heterogeneity in modelled biomass abundance as well as the statistics of small values outside of the productive stream channels. Further ground validation efforts in areas of low photosynthetic biology abundances are ongoing and will help to constrain this model uncertainty.

Power et al. (2020) also utilized remote sensing to derive total organic carbon abundance in the Canada ASPA by calculating the Normalized Difference Vegetation Index (NDVI) and validating these values with in situ validation points of ground sampling and surveying. They estimated a total organic carbon abundance of 21,715 kg C in the Canada ASPA using satellite data from January of 2018, which is slightly more than half of our estimated value of 38,559.1 kg C in December of 2018. The discrepancy between our study and that of Power et al. (2020) is potentially due to their use of a NDVI detection threshold that minimized the number of pixels aggregated into their overall calculation. It is also unclear how the activity (and, comparably, the detectability) of photosynthetic biomass outside of stream channels changes over time with changes in environmental conditions (e.g., weather). Similar to the activity of photosynthetic vegetation in many terrestrial landscapes, it is possible that soil communities outside of the stream channels undergo a "green-up" as conditions allow, which may also result in significant spatial and temporal heterogeneity in identified biological materials between different dates. Additional work is ongoing to characterize the spectral variability in typical Taylor Valley soils as a function of environmental conditions and associated biological and photosynthetic activity.

This work allows for comparisons between total standing biomass in the MDV and other terrestrial ecosystems. For example, the density of actively photosynthesizing biomass recorded in the Fryxell basin in December of 2018 using our remote sensing techniques $(26.7 \pm 2.9 \text{ g m}^{-2})$ is less than 5% of live aboveground biomass measured in the plains of the Sonoran Desert near Hermosillo, Mexico $(578.0 \pm 294.6 \text{ g m}^{-2})$, which contains broadly spaced ironwood trees, palo verde trees, and shrubs (Búrquez et al. 2010). Interestingly, our orbital estimate of biomass in Grid 3 in the Flush of Canada Stream (355.2 \pm 38.0 g m⁻²) is 61.5% that of the biomass density found in the Sonoran Plains (Búrquez et al. 2010) and equivalent to biomass found in grass-dominated meadows (Proulx et al. 2015). These comparisons demonstrate that biological "hot spots" in the Fryxell basin contain significant amounts of biological materials, challenging the common perception that the MDV are barren and lifeless environments. Carbon fixation can also be estimated using previously calculated fixation rates of relevant microbial mats. Novis et al. (2007) estimated carbon fixation rates in healthy black microbial mats in the MDV at 21 g m⁻² year⁻¹ which, assuming a comparable rate for all biological organisms identified in this investigation, would amount to 64,074.6 kg C year⁻¹ for the entirety of the Fryxell basin, or roughly equivalent to 5 ha of tropical rainforest (Soepadmo 1993).

This work provides a critically important, calibrated, standardized, repeatable, and accurate means of remotely quantifying photosynthetically active biomass in terrestrial ecosystems of the MDV (Figure 11). It is now possible to apply these techniques to past, present, and future remote sensing data to investigate critical relationships between environmental drivers and biological response in one of the most remote locations on Earth. These techniques will help to provide localized biological assessments made by the McMurdo Dry Valley Long-Term Ecological Research (MCM LTER) Program with broader spatial and temporal context. This critical capability is the necessary link to understand these extremophile ecosystems and predict their responses to the changing environment. This work also demonstrates the utility of orbital multispectral remote sensing in deriving accurate spatial and temporal estimates of terrestrial biomass in the remote MDV of Antarctica. Despite the episodic nature of water availability and photosynthesis, the scarcity of photosynthetic communities, and their unique adaptations designed to protect them from the harsh surface conditions, it is possible to rapidly and accurately measure surface biomass on a per pixel basis. Together with the 30+ year records of meteorological and hydrological data collected and archived by the MCM LTER Program, application of these techniques to past and future orbital data will facilitate temporal studies of ecosystem dynamics in the MDV and particularly how they respond to climatic and hydrological variability.

6.0 Conclusions

Our work fills an important gap in correlating localized measurements of photosynthetic biological activity and biomass to regional-scale estimates of these important ecological properties. Through the assembly of a unique spectral endmember library, the validation of our unmixing efforts using coincident field measurements, and the regional extrapolation of this technique, we have demonstrated the value of remote sensing data to not only identify local biological activity, but to serve as a valuable monitor for regional ecological processes associated with photoautotrophic communities. Work is ongoing to expand these methods to broader image suites, to identify future sites of remote investigation, and to identify where additional ground validation and/or field work is necessary to expand our confidence in these techniques. Ongoing and future studies of ecological processes in the MDV should utilize high-resolution multispectral remote sensing data and the techniques developed here for both local characterization and for understanding regional ecological context.



Acknowledgements

General: The authors would like to thank the Polar Geospatial Center (PGC) and the National Geospatial Intelligence Agency (NGA) for providing access to the remote sensing data. We would also like to thank the National Science Foundation (NSF) and the U.S. Antarctic Program (USAP) for access to field locations. Lastly, we would like to thank the members of the McMurdo Dry Valleys Long-Term Ecological Research (MCM LTER) Program for helpful discussions regarding this work and the ecological implications of our results.

Author Contributions

MRS was the primary author of this manuscript and led the field research and data analysis that is presented here. JEB and MNG provided regional ecological insight and assisted with data interpretation and field work. SRB and SNP are graduate students associated with this project and assisted with field work, data analysis, and spectral and ecological interpretations. LFS and ERS contributed significantly to the planning and execution of the field work and sample analyses, and in the writing and revision process.

Disclosure statement

No potential conflict of interest was reported by the author(s).

Data Availability

Satellite images are available to NSF OPP investigators through a cooperative agreement between NSF, the Polar Geospatial Center, and the National Geospatial Intelligence Agency, with direct lines of communication with DigitalGlobe, Inc. All other data required to reproduce our results are either provided in Supplemental Materials or are available upon request to MRS.

Funding

This work was funded by the National Science Foundation (NSF) Office of Polar Programs Award No. 1745053. Additional funding for co-authors include the McMurdo Dry Valleys Long-Term Ecological Research Program (NSF OPP Award No. 1637708) and Northern Arizona University.

ORCID

Mark R. Salvatore (b) http://orcid.org/0000-0002-1551-8342 John E. Barrett (h) http://orcid.org/0000-0002-7610-0505 Schuyler R. Borges (i) http://orcid.org/0000-0002-4565-6463 Sarah N. Power (h) http://orcid.org/0000-0002-4863-290X Lee F. Stanish (b) http://orcid.org/0000-0002-9775-6861 Eric R. Sokol (i) http://orcid.org/0000-0001-5952-0917 Michael N. Gooseff (b) http://orcid.org/0000-0003-4322-8315

References

Adams, J. B., M. O. Smith, and A. R. Gillespie. 1993. "Imaging spectroscopy: Interpretation based on spectral mixture analysis." In Topics in, edited by I. V. Remote Sensing, A. C. Remote Geochemical, M. Pieters, and P. A. J. Englert, 145–166. Cambridge: Cambridge University Press.



- Alger, A. S., D. M. McKnight, S. A. Spaulding, C. M. Tate, G. H. Shupe, K. A. Welch, R. Edwards, E. D. Andrews, and H. R. House. 1997. "Ecological processes in a cold desert ecosystem: The abundance and species distribution of algal mats in glacial meltwater streams in Taylor Valley, Antarctica." Institute of Arctic and Alpine Research Occasional Paper 51.
- Ball, B. A., and R. A. Virginia. 2014. "The ecological role of moss in a polar desert: Implications for aboveground-belowground and terrestrial-aquatic linkages." *Polar Biology* 37 (5): 651–664. doi:10.1007/s00300-014-1465-2.
- Barrett, J. E., R. A. Virginia, A. N. Parsons, and D. H. Wall. 2006. "Soil carbon turnover in the McMurdo Dry Valleys, Antarctica." *Soil biology & biochemistry* 38 (10): 3065–3082. doi:10.1016/j. soilbio.2006.03.025.
- Barták, M., J. Hazdrová, K. Skácelová, and J. Hájek. 2016. "Dehydration-induced responses of primary photosynthetic processes and spectral reflectance indices in Antarctic." *Nostoc commune. Czech Polar Reports* 6 (1): 87–95. doi:10.5817/CPR2016-1-9.
- Burkins, M. B., R. A. Virginia, and D. H. Wall. 2001. "Organic carbon cycling in Taylor Valley, Antarctica: Quantifying soil reservoirs and soil respiration." *Global Change Biology* 7. doi:10.1046/j.1365-2486.2001.00393.x.
- Búrquez, A., A. Martínez-Yrízar, S. Núñez, T. Quintero, and A. Aparicio. 2010. "Aboveground biomass in three Sonoran Desert communities: Variability within and among sites using replicated plot harvesting." *Journal of Arid Environments* 74 (10): 1240–1247. doi:10.1016/j. aridenv.2010.04.004.
- Clark, R. N., T. V. V. King, M. Klejwa, G. A. Swayze, and N. Vergo. 1990. "High spectral resolution reflectance spectroscopy of minerals." *Journal of Geophysical Research* 95 (B8): 12653–12680. doi:10.1029/JB095iB08p12653.
- Conovitz, P. A., D. M. McKnight, L. H. MacDonald, A. G. Fountain, and H. R. House. 1998. "Hydrologic processes influencing streamflow variation in Fryxell basin, Antarctica." In *Ecosystem Dynamics in a Polar Desert: The McMurdo Dry* Valleys, *Antarctica*. Antarctic Research Series 73, edited by J. C. Priscu, 93–108. Washington, DC: AGU.
- Cullis, J. D. S., L. F. Stanish, and D. M. McKnight. 2014. "Diel flow pulses drive particulate organic matter transport from microbial mats in a glacial meltwater stream in the McMurdo Dry Valleys." Water Resources Research 50 (1): 86–97. doi:10.1002/2013WR014061.
- Doran, P. T., C. P. McKay, G. D. Clow, G. L. Dana, A. G. Fountain, T. Nylen, and W. B. Lyons. 2002. "Valley floor climate observations from the McMurdo Dry Valleys, Antarctica, 1986 2000." *Journal of Geophysical Research* 107. doi:10.1029/2001JD002045.
- Fountain, A. G., W. B. Lyons, M. B. Burkins, G. L. Dana, P. T. Doran, K. J. Lewis, D. M. McKnight, et al. 1999. "Physical controls on the Taylor Valley ecosystem, Antarctica." *BioScience* 49 (12): 961–971. doi:10.1525/bisi.1999.49.12.961.
- Gooseff, M. N., J. E. Barrett, B. J. Adams, P. T. Doran, A. G. Fountain, W. B. Lyons, D. M. McKnight, et al. 2017. "Decadal ecosystem response to an anomalous melt season in a polar desert in Antarctica." *Nature Ecology and Evolution* 1 (9): 1334–1338. doi:10.10138/s41559-017-0253-0.
- Hapke, B. 1993. *Theory of Reflectance and Emittance Spectroscopy*, 513. Cambridge, UK: . Cambridge University Press.
- Hawes, I., C. Howard-Williams, and W. F. Vincent. 1992. "Desiccation and recovery of Antarctic cyanobacterial mats." *Polar Biology* 12 (6–7): 587–594. doi:10.1007/BF00236981.
- Kohler, T. J., L. F. Stanish, S. W. Crisp, J. C. Koch, D. Liptzin, J. L. Baeseman, and D. M. McKnight. 2015. "Life in the main channel: Long-term hydrologic control of microbial mat abundance in McMurdo Dry Valley streams, Antarctica." *Ecosystems* 18 (2): 310–327. doi:10.1007/s10021-014-9829-6.
- Lawson, C. L., and R. J. Hanson. 1974. *Solving Least-Squares Problems*, 340. Englewood Cliffs, NJ: Prentice-Hall.
- McKnight, D. M., D. K. Niyogi, A. S. Alger, A. Bomblies, P. A. Conovitz, and C. M. Tate. 1999. "Dry valley streams in Antarctica: Ecosystems waiting for water." *BioScience* 49 (12): 985–995. doi:10.1525/bisi.1999.49.12.985.
- McKnight, D. M., and C. M. Tate. 1997. "Canada Stream: A glacial meltwater stream in Taylor Valley, South Victoria Land, Antarctica." *Journal of the North American Benthological Society* 16 (1): 14–17. doi:10.2307/1468224.



- McKnight, D. M., C. M. Tate, E. D. Andrews, D. K. Niyogi, K. Cozzetto, K. Welch, W. B. Lyons, and D. G. Capone. 2007. "Reactivation of a cryptobiotic stream ecosystem in the McMurdo Dry Valleys, Antarctica: A long-term geomorphological experiment." Geomorphology 89 (1-2): 186-204. doi:10.1016/j.geomorph.2006.07.025.
- Michaud, A. B., M. Šabacká, and J. C. Priscu. 2012. "Cyanobacterial diversity across landscape units in a polar desert: Taylor Valley, Antarctica." FEMS Microbial Ecology 82 (2): 268-278. doi:10.1111/ j.1574-6941.2012.01297.x.
- Moorhead, D. L., P. T. Doran, A. G. Fountain, W. B. Lyons, D. M. McKnight, J. C. Priscu, R. A. Virginia, and D. H. Wall. 1999. "Ecological legacies: Impacts on the ecosystems of the McMurdo Dry Valleys." BioScience 49 (12): 1009–1019. doi:10.1525/bisi.1999.49.12.1009.
- Niederberger, T. D., E. M. Bottos, J. A. Sohm, T. Gunderson, A. Parker, K. J. Coyne, D. G. Capone, E. J. Carpenter, and S. C. Cary. 2019. "Rapid microbial dynamics in response to an induced wetting event in Antarctic Dry Valley soils." Frontiers in Microbiology 10. doi:10.3389/fmicb.2019.00621.
- Nkem, J. N., D. H. Wall, R. A. Virginia, J. E. Barrett, E. J. Broos, B. J. Adams, and D. L. Porazinska. 2006. "Wind dispersal of soil invertebrates in the McMurdo Dry Valleys, Antarctica." Polar Biology 29 (4): 346-352. doi:10.1007/s00300-005-0061-x.
- Novis, P. M., D. Whitehead, E. G. Gregorich, J. E. Hunt, A. D. Sparrow, D. W. Hopkins, B. Elberling, and L. G. Greenfield. 2007. "Annual carbon fixation in terrestrial populations of Nostoc commune (Cyanobacteria) from an Antarctic dry valley is driven by temperature regime." Global Change Biology 13 (6): 1224-1237. doi:10.1111/j.1365-2486.2007.01354.x.
- Peddle, D. R., F. G. Hall, and E. F. LeDrew. 1999. "Spectral mixture analysis and geometric-optical reflectance modeling of boreal forest biophysical structure." Remote Sensing of Environment 67 (3): 288-297. doi:10.1016/S0034-4257(98)00090-X.
- Power, S. N., M. R. Salvatore, E. R. Sokol, L. F. Stanish, and J. E. Barrett. 2020. "Estimating microbial mat biomass in the McMurdo Dry Valleys, Antarctica using satellite imagery and ground surveys." Polar Biology 43 (11): 1753-1767. doi:10.1007/s00300-020-02742-y.
- Proulx, R., G. Rheault, L. Bonin, I. T. Roca, C. A. Martin, L. Desrochers, and I. Seiferling. 2015. "How much biomass do plant communities pack per unit volume?." PeerJ 3: e849. doi:10.7717/ peeri.849.
- Ramsey, M. S., and P. R. Christensen. 1998. "Mineral abundance determination: Quantitative deconvolution of thermal emission spectra." Journal of Geophysical Research 103 (B1): 577-596. doi:10.1029/97JB02784.
- Roberts, D. A., J. B. Adams, and M. O. Smith. 1993. "Green vegetation, non-photosynthetic vegetation and soils in AVIRIS data." Remote Sensing of Environment 44 (2-3): 255-269. doi:10.1016/0034-4257(93)90020-X.
- Rodríguez-Caballero, E., P. Escribano, and Y. Cantón. 2014. "Advanced image processing methods as a tool to map and quantify different types of biological soil crust." ISPRS Journal of Photogrammetry and Remote Sensing 90: 59-67. doi:10.1016/j.isprsjprs.2014.02.002.
- Salvatore, M. R. 2015. "High-resolution compositional remote sensing of the Transantarctic Mountains: Application to the WorldView-2 dataset." Antarctic Science 27 (5): 473-491. doi:10.1017/S095410201500019X.
- Salvatore, M. R., S. R. Borges, J. E. Barrett, E. R. Sokol, L. F. Stanish, S. N. Power, and P. Morin. 2020. "Remote characterization of photosynthetic communities in the Fryxell basin of Taylor Valley, Antarctica." Antarctic Science 32 (4): 255-270. doi:10.1017/S0954102020000176.
- Schwarz, A. M. J., T. G. A. Green, and R. D. Seppelt. 1992. "Terrestrial vegetation at Canada Glacier, southern Victoria Land, Antarctica." Polar Biology 12 (3-4): 397-404. doi:10.1007/BF00243110.
- Seppelt, R. D., T. G. A. Green, A.-M. J. Schwarz, and A. Frost. 1992. "Extreme southern locations for moss sporophytes in Antarctica." Antarctic Science 4 (1): 37–39. doi:10.1017/ S0954102092000087.
- Soepadmo, E. 1993. "Tropical rain forests as carbon sinks." Chemosphere 27 (6): 1025-1039. doi:10.1016/0045-6535(93)90066-E.



- Takacs-Vesbach, C., L. Zeglin, J. E. Barrett, M. N. Gooseff, and J. C. Priscu. 2010. "Factors promoting microbial diversity in the McMurdo Dry Valleys, Antarctica." In In Life in Antarctic Deserts and Other Cold Dry Environments, edited by P. T. Doran, W. B. Lyons, and D. M. McKnight, 221–257. Cambridge: Cambridge University Press.
- Thuillier, G. 2003. "The solar spectral irradiance from 200 to 2400 nm as measured by SOLSPEC Spectrometer from the ATLAS 123 and EURECA missions." Solar Physics 214 (1): 1–22. doi:10.1023/ A:1024048429145.
- Trnková, K., and M. Barták. 2017. "Desiccation-induced changes in photochemical processes of photosynthesis and spectral reflectance in Nostoc commune (Cyanobacteria, Nostocales) colonies from polar regions." Psychological Research 65 (1): 44–50. doi:10.1111/pre.12157.
- Updike, T., and C. Comp. 2010. "Radiometric use of WorldView-2 imagery." Technical Note. DigitalGlobe, Inc., Longmont, CO. 16 p.
- Van Horn, D. J., C. R. Wolf, D. R. Colman, X. Jiang, T. J. Kohler, D. M. McKnight, L. F. Stanish, T. Yazzie, C. D. Takacs-Vesbach, and M. Häggblom. 2016. "Patterns of bacterial biodiversity in the glacial meltwater streams of the McMurdo Dry Valleys, Antarctica." FEMS Microbiology Ecology 92 (10): fiw148. doi:10.1093/femsec/fiw148.
- Vincent, W. F., and C. Howard-Williams. 1986. "Antarctic stream ecosystems: Physiological ecology of a blue-green algal epilithon." Freshwater Biology 16 (2): 219-233. doi:10.1111/j.1365-2427.1986.
- Virginia, R. A., and D. H. Wall. 1999. "How soils structure communities in the Antarctic Dry Valleys." BioScience 49 (12): 973-983. doi:10.1525/bisi.1999.49.12.973.
- Wall, D., and R. A. Virginia. 2005. "McMurdo Dry Valleys LTER: Soil Elevational Transect Experiment." Environmental Data Initiative, doi:10.6073/pasta/33c859342a0447b8f67fc71fada305b9.
- Wlostowski, A. N., M. N. Gooseff, D. M. McKnight, C. Jaros, and W. B. Lyons. 2016. "Patterns of hydrological connectivity in the McMurdo Dry Valleys, Antarctica: A synthesis of 20 years of hydrologic data." Hydrological Processes 30 (17): 2958–2975. doi:10.1002/hyp.10818.
- Wynn-Williams, D. D. 1996. "Antarctic microbial diversity: The basis of polar ecosystem processes." Biodiversity and conservation 5 (11): 1271–1293. doi:10.1007/BF00051979.
- Zhang, H., Y. Yang, W. Jin, C. Liu, and W. Hsu. 2014. "Effects of Spectralon absorption on reflectance spectra of typical planetary surface analog materials." Optics Express 22 (18): 21280-21291. doi:10.1364/OE.22.021280.
- Zhang, L., A. D. Jungblut, I. Hawes, D. T. Anderson, D. Y. Sumner, and T. J. Mackey. 2015. "Cyanobacterial diversity in benthic mats of the McMurdo Dry Valley lakes, Antarctica." Polar Biology 38 (8): 1097-1110. doi:10.1007/s00300-015-1669-0.